Available online at www.sciencedirect.com
SCIENCE DIRECT®
Optical Materials 26 (2004) 375–383
OPTICAL Materials
www.elsevier.com/locate/optmat

Growth of Yb^{3+}-doped $YLiF_4$ laser crystal by the Czochralski method. Attempt of Yb^{3+} energy level assignment and estimation of the laser potentiality

A. Bensalah [a,b], Y. Guyot [a], M. Ito [a], A. Brenier [a], H. Sato [b], T. Fukuda [b], G. Boulon [a,b,*]

[a] *Physics and Chemistry of Luminescent Materials, UMR 5620 CNRS, Claude Bernard/Lyon1 University, 69622 Villeurbanne, France*
[b] *Institute of Multidisciplinary Research for Advanced Materials, Tohoku University, 2-1-1 Aobaku, Katahira Sendai 980-8577, Japan*

Received 24 July 2003; accepted 15 September 2003
Available online 9 April 2004

Abstract

$YLiF_4$ (YLF) single crystals undoped and Yb^{3+}-doped with different concentrations were grown by the Czochralski technique under CF_4 atmosphere. Detailed analysis of Yb^{3+}-doped YLF spectroscopy were made to contribute to the determination of energy levels in this host. We are dealing with temperature and concentration dependences of both π and σ polarizations of the infrared (IR) absorption and emission spectra. Raman spectra were also used to give an attempt of interpretation of electronic and vibronic levels. The radiative energy transfer (self-trapping) and strong phonon–electron coupling make the assignment of Yb^{3+} energy levels difficult. Evaluation of the laser potentiality of this fluoride host is also presented.

Keywords: Laser crystals; Yb^{3+}-doped $YLiF_4$; Energy levels

1. Introduction

In the latest years, with advances of high performance in GaAs laser diode with wavelength between 0.9 and 1.1 μm [1], interest in Yb^{3+}-doped materials has been increasing for application in high efficiency and high power diode pumped laser systems [2]. The ytterbium ion is ideally suited for diode pumping since it has the simplest energy level scheme, among the rare earth active ions, consisting in only two levels: the $^2F_{7/2}$ ground state and the $^2F_{5/2}$ excited state. This simple electronic structure results in several advantages, comparing with Nd^{3+} ion for instance, such us no excited state absorption, no absorption in the visible range, no cross-relaxation process and no more up-conversion or any internal mechanism able to reduce the effective laser cross-section. In addition, the intense and broad Yb^{3+} absorption lines are well suited for IR In GaAs diode laser pumping, the broad emission band allows the generation of ultra-short pulses and the small quantum defect between absorption and emission wavelengths, leads to a low thermal load (11% relative to 30–40% in Nd^{3+}-doped laser hosts).

Among the different hosts possible for laser application, fluorides single crystals are interesting because of their high transparency in a wide wavelength region from the VUV to the IR, lower refractive index limiting non-linear effects under intense laser sources pumping and low phonon energy, which increase the radiative transfer probability of the active ions. Moreover, our group has recently investigated spectroscopic properties of several Yb^{3+}-doped single crystal oxides and a new general method of evaluation was pointed out depending on the oscillator or the amplifier regimes [3,4]. In order to be completed this study should include fluoride single crystals, another crystal family very useful for optical applications like laser sources. In this paper, spectroscopic properties of Yb^{3+} ion are reported in the

* Corresponding author.
E-mail address: georges.boulon@pcml.univ-lyon1.fr (G. Boulon).

0925-3467/$ - see front matter © 2004 Elsevier B.V. All rights reserved.
doi:10.1016/j.optmat.2003.09.015

fluoride host $YLiF_4$ (YLF) grown by the Czochralski method.

2. Experimental

Crystal growth was performed in a vacuum-tight Czochralski (CZ) system equipped with an automatic diameter control system. The resistive heater and thermal insulators were made of high-purity graphite. The starting materials were prepared from high-purity commercial fluoride powders of LiF and YF_3, (>99.99%). As dopants, YbF_3 powders of high purity (>99.99%) was used. Since the congruent composition of YLF compound is slightly shifted from the stoichiometric one, the starting composition was prepared in the ratio of 52% LiF: 48% YF_3. The basic compounds and the dopants were melted in a platinum crucible with 60 mm in diameter. The pulling rate was 1 mm/h and the rotation rate was 15 rpm. Growth orientations were controlled using the *a*-axis oriented undoped YLF seed crystal. Prior to filling with gas and melting the charge, the growth chamber was evacuated to 10^{-4} Pa and heated to 700 °C for a period of 12 h. Such treatment was carried out to eliminate water and/or oxygen from the chamber and the starting materials [5]. High-purity CF_4 gas (99.9999%) was slowly introduced into the furnace. The mixtures were melted under this atmosphere. After growth, the crystals were cooled down to room temperature at a rate of 30 °C/h.

The crystals were sectioned longitudinally to measure the composition over the length of the boule. The Yb^{3+} doping level in the grown crystals was measured by the inductively coupled plasma technique. Powder X-ray diffraction (XRD) measurements for lattice parameter determinations were carried out on a Rigaku diffractometer (Rint model), operated at 40 kV and 40 mA in the 2θ range of 10–80°.

Samples for spectroscopic measurements were cut parallel to the optical *c*-axis and polished. Absorption spectra were recorded with a spectrophotometer Perkin–Elmer lambda 9000 equipped with a cryostat allowing measurements between 12 K and room temperature. Excitation of the Yb^{3+} fluorescence was performed with a frequency doubled Nd:YAG laser (10 ns, 10 Hz) pumping a Quantel two-amplifier-stage, dye laser containing a mixture of DCM and LD698 and followed by a hydrogen Raman cell shifter to generate a beam in the 920–960 nm range. The specific infrared fluorescence is selected by using a Jobin Yvon HRS1 monochromator fit with a 600 grooves/mm grating blazed at 1 μm. The signal is detected by a slow North Coast germanium cell, cooled by liquid nitrogen, and sent into a Stanford boxcar averager SRS 250. The decay kinetics were recorded with a Lecroy LT 342 digital oscilloscope connected to a fast North Coast germanium cell.

3. Results and discussion

3.1. Crystal growth and structural characterization

When powder raw materials were melted, a black scum was observed floating on the melt surface. This film is due to the oxygen and carbon contamination of the raw materials [6]. However, a clean and transparent melt was obtained after removing the scum by scraping the solidified surface and subsequently re-melting the compound. Fig. 1 shows the as-grown 10% Yb^{3+}-doped YLF single crystal with dimensions of 18 mm in diameter and 70 mm in length. Obtained crystals were transparent free from cracks, bubbles and inclusions.

YLF compound has a scheelite structure with tetragonal system. It crystallises in $I4_1/a$ (C^6_4h) space group, lattice parameters $a = 5.155$ Å and $c = 10.68$ Å. While doping with Yb^{3+} ion in this host it will substitute the dodecahedral site of Y^{3+}. Since this host ion and the Yb^{3+} dopant have the same charge state and comparable ionic radius (0.977 and 0.985 Å respectively), we expected that the dopant would easily enter this matrix. Indeed, we measured the concentration of Yb^{3+} ion in the grown crystal and the uniformity of the Yb^{3+} dopant distribution along the crystal growth axis was checked, with five samples taken along the crystal growth axis. An example is given in Fig. 2(a) for the highest concentration of Yb^{3+} in YLF (10% Yb-doped YLF). The distribution coefficient of Yb (k_{eff}) in this single crystal was estimated to be 0.96. This value was calculated using the normal freezing equation: $C_s = C_0 k_{\text{eff}}(1-g)^{k-1}_{\text{eff}}$ [7], where C_s is the measured concentration in the samples, C_0 is the initial concentration in the melt, g is the melt solidified fraction, and k_{eff} is the effective distribution coefficient of the dopant ion. The distribution coefficient is close to unity, which means that Yb^{3+} efficiently entered the YLF host as was expected. Dependence of the lattice parameters *a* and *c* on the solidification fraction for the 10% Yb-doped YLF was

Fig. 1. 10% Yb^{3+}-doped $YLiF_4$ single crystal with 1 in. in diameter grown by the Czochralski method.

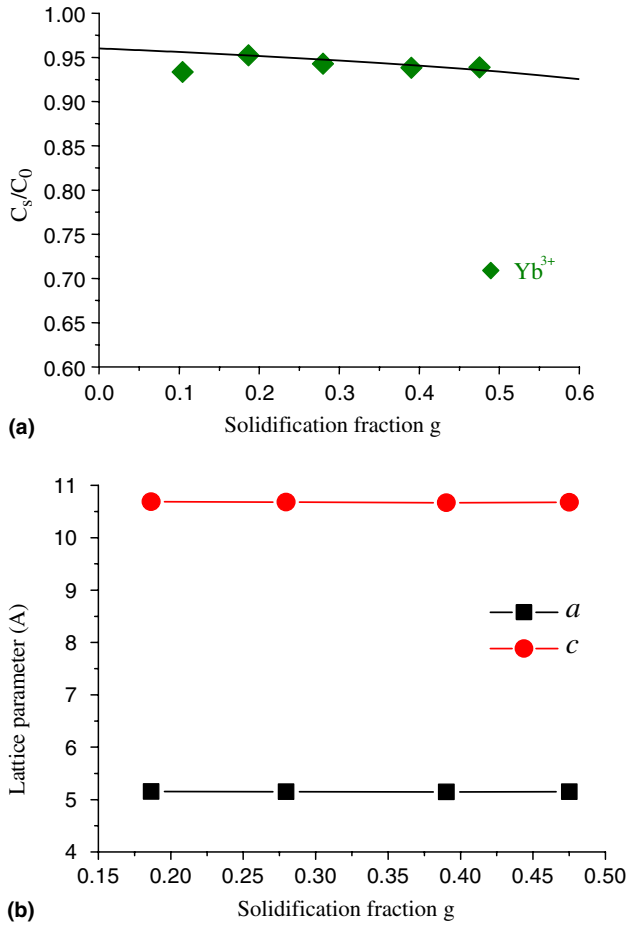

Fig. 2. (a) Distribution of Yb^{3+} along the growth axis in the 10% Yb^{3+}-doped $YLiF_4$, (b) dependence of the lattice parameters a and c on the solidification fraction for the 10% Yb-doped YLiF4.

measured as well and is shown in Fig. 2(b). The variation of the lattice parameters is constant and this accords well with the size of the ionic radius of the dopant and the host ion.

3.2. Absorption and emission spectra: attempt of the assignment of Yb^{3+} energy levels:

3.2.1. Assignment of the $1 \leftrightarrow 5$ resonant 0-phonon line as a reference

To characterize the electric-dipole transitions for uniaxial crystal, two orientations are needed: the π spectra with $E \| c$ and the σ spectra with $E \perp c$. The absorption cross-sections were easy to measure from optical density, thickness and concentration of the sample whereas the emission cross-sections were obtained from the Fuchtbauer–Ladenburg method. The decay times were measured at RT and 12 K for 0.5 and 10% Yb^{3+} as reported in Table 1. The polarized absorption and emission (π and σ) spectra of the 0.5% Yb^{3+}-doped YLF at room temperature (RT) under pumping of the highest Stark level ($1 \rightarrow 7$) at 930 nm are

Table 1
Decay time values of Yb^{3+} $^2F_{5/2}$ excited level in $YLiF_4$

Sample	Decay time (ms)
10% Yb:YLF RT	3.18
10% Yb:YLF (12 K)	2.25
0.5% Yb:YLF RT	2.14
0.5% Yb:YLF (12 K)	1.94

plotted in Fig. 3. First of all, with respect to other Yb^{3+}-doped crystals, the crystal field intensity is much weaker in this host: absorption spectra start only at around 920 nm whereas emission spectra only extend till 1070 nm at RT. We also observe a large overlap between absorption and emission spectra. Several bands can be seen in both absorption and emission due to the different transitions between the ground and the excited state of Yb^{3+} ion. The energy-level scheme of Yb^{3+} contains only two multiplet manifolds: the ground $^2F_{7/2}$ state and the excited $^2F_{5/2}$ state. Stark levels are distributed in the two manifolds and labelled from 1 to 4 in the ground state and from 5 to 7 in the excited state from the lowest to the highest energy as can be seen in the inset of Fig. 3. However, due to the strong electron–photon coupling of Yb^{3+} ion, additional peaks appear and it is then difficult to ascribe the different absorption and emission lines in YLF host especially at RT. The highest values of absorption and emission cross-section at RT in π polarization, are 0.9×10^{-20} cm^2 at 960 nm ($E//c$) and 1.3×10^{-20} cm^2 at 995 nm ($E//c$) respectively that are in a good agreement with results reported in literature [8]. In absorption spectra, especially in the π polarization at RT, the transitions from the $^2F_{7/2}$ ground state thermally populated Stark levels are clearly seen and fit well with the corresponding emission transitions. Indeed, the observed peaks are the result of absorption from all 1, 2, 3 and even 4 populated Stark levels.

In order to point out the Yb^{3+} concentration effect on the fluorescence, we present together, in Fig. 4, the polarized emissions at RT of the 0.5% and the 10% Yb-doped YLF. With the increase of Yb^{3+} concentration in YLF we can clearly see the re-absorption of only the resonant transitions by radiative energy transfer between Yb^{3+} ions, which results in a decrease of the emission cross-sections. This feature is especially observed for the band at 960 nm since it has the strongest absorption cross-section at RT. This re-absorption effect by self-trapping process of the resonant lines was also observed in other hosts such us garnets [9,10] and sesquioxides [11].

The $1 \leftrightarrow 5$ 0-phonon line, which is defined to be the energy separation between the lowest Stark levels of each manifold, was very difficult to ascribe at 972 nm, especially because its absorption and emission cross-section values are the lowest ones with same value of 0.38×10^{-20} cm^2 at RT in π polarization (Fig. 3). Usually at RT, in Yb^{3+}-doped materials the $1 \leftrightarrow 5$ transition

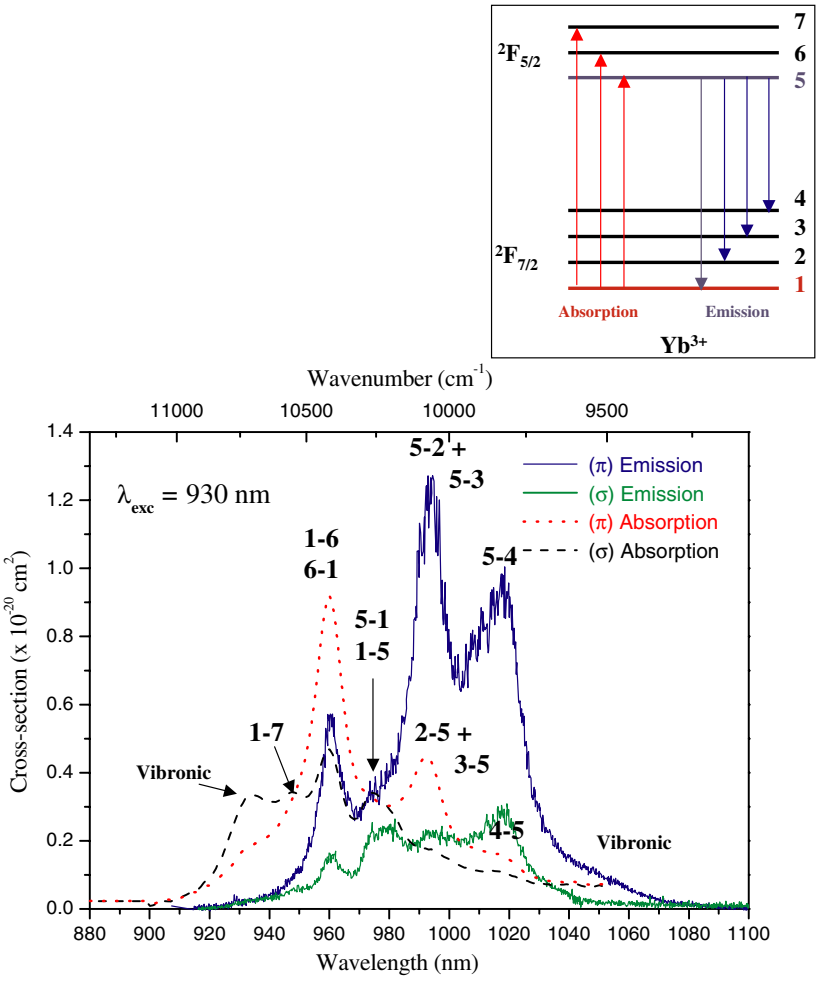

Fig. 3. Polarized absorption and emission cross-section at room-temperature of 0.5% Yb^{3+}-doped $YLiF_4$.

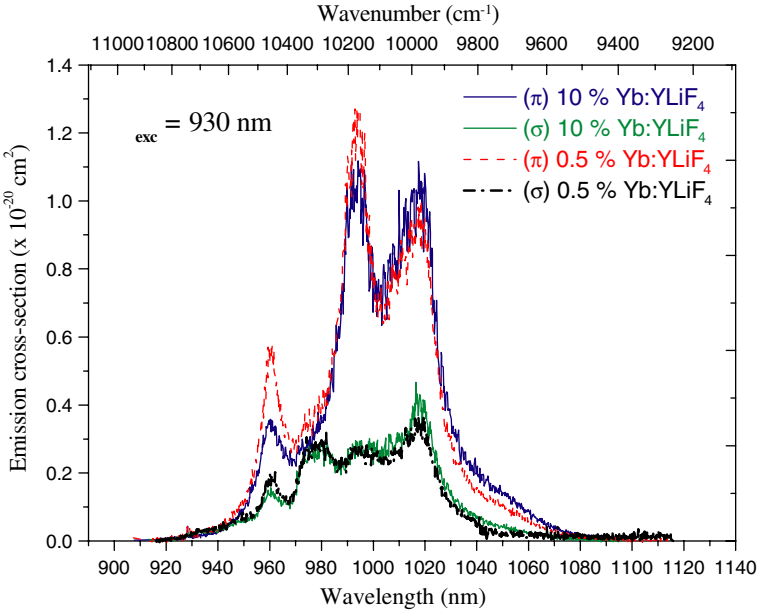

Fig. 4. Polarized emission cross-section of 10% and 0.5% Yb^{3+}-doped $YLiF_4$.

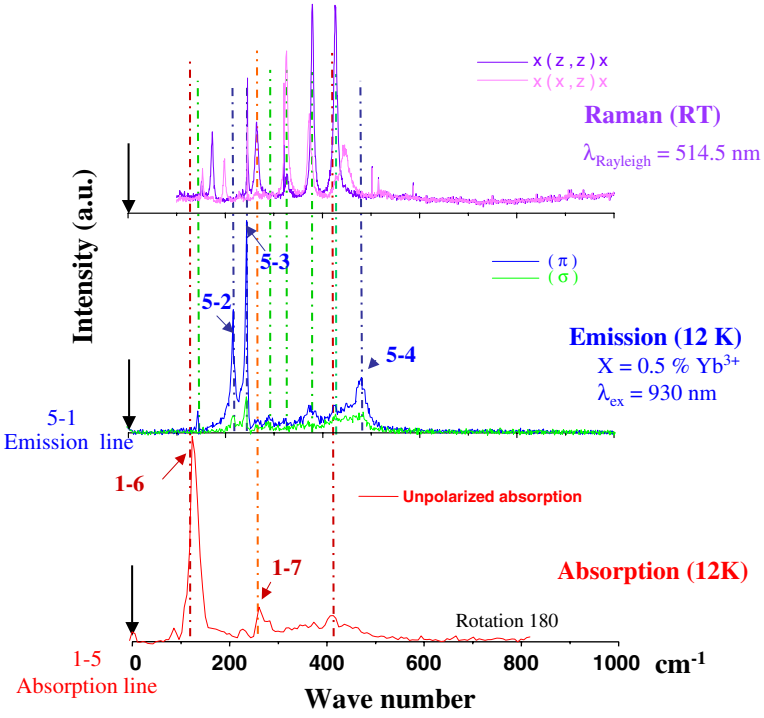

Fig. 5. Interpretation of Yb^{3+} transitions in 0.5% Yb-doped $YLiF_4$ with the help of absorption, emission and Raman spectra.

has higher cross-sections comparing with the $1 \leftrightarrow 6$ transition whereas at low temperature it is the opposite. However, in this case, since the emission cross-section at 12 K (Fig. 6) under excitation of the $1 \rightarrow 7$ line, shows that the peak at 960 nm disappears totally while the one at 972 nm is very small (0.26×10^{-20} cm^2) but still existing, it confirms the 0-phonon line of the $5 \rightarrow 1$ emission transition at 972 nm. Another confirmation is pointed out by the low temperature emission spectrum as shown in Fig. 7 for 0.5% Yb:YLF grown not by the CZ method but by the LHPG (Laser Heated Pedestal Growth) method [3–11]. The $5 \rightarrow 1$ emission transition is clearly seen at 972 nm in Fig. 7. Consequently, we can conclude that this line is our reference for Yb^{3+} spectroscopy in YLF, and add that a special care is needed to assign Yb^{3+} absorption and emission transitions in YLF.

3.2.2. Attempt to recognize electronic and vibronic transitions

The strong interaction of Yb^{3+} ions with the lattice vibrations give rise to strong vibronic sidebands or even to supplementary Stark level splitting due to the resonance between Stark levels and phonon [9,12,13] which can easily be mistaken for the assignment of electronic transitions. Considering the 0-phonon line at 972 nm, in order to aid our interpretation of the electronic levels, we have used a simple experimental method and compared the absorption and emission spectra at low temperature with those of the Raman spectra to select both electronic and vibronic transitions. Then, we are admitting the hypothesis that Raman spectrum should reflect vibronic structure accompanying each resonant 0-phonon line electronic transition. In Fig. 5, polarized luminescence and unpolarized absorption spectra are reported at 12 K. The polarized Raman spectra were only recorded at RT. These spectra were adjusted to the same energy scale, by taking the origin of the absorption and the emission at the $1 \leftrightarrow 5$ transition, in coincidence with the Rayleigh line of the Ar-laser (514.5 nm) used to record the Raman spectra. By rotating the absorption spectrum around the origin of 180°, we get a direct comparison with both emission and Raman spectra, which are then drawn to the lowest frequency side. Thus, by comparing these three spectra, we should distinguish the vibronic lines, which are common to the 3 spectra whereas the energy positions of the different Stark levels are not seen in the Raman spectrum.

3.2.2.1. Absorption spectra. The absorption peak at around 126 cm^{-1} (10 416 cm^{-1}) does not overlap with the vibronic spectrum, whereas there is a strong overlapping of the other peaks in the range 200–400 cm^{-1}. The assignment of this line is probably the $1 \rightarrow 6$ transition in agreement with the interpretation given for the first time by Morrison et al. [14,15], which is since considered as a reference and Lupei et al. [16].

Concerning the $1 \rightarrow 7$ transition, the interpretation is rather delicate operation since we observe two peaks located at 10 554 and 10 706 cm^{-1} which correspond at 260 and at 416 cm^{-1} respectively above the 5 level. Consequently, the $1 \rightarrow 7$ absorption transition can be assigned at one of this two positions. In order to

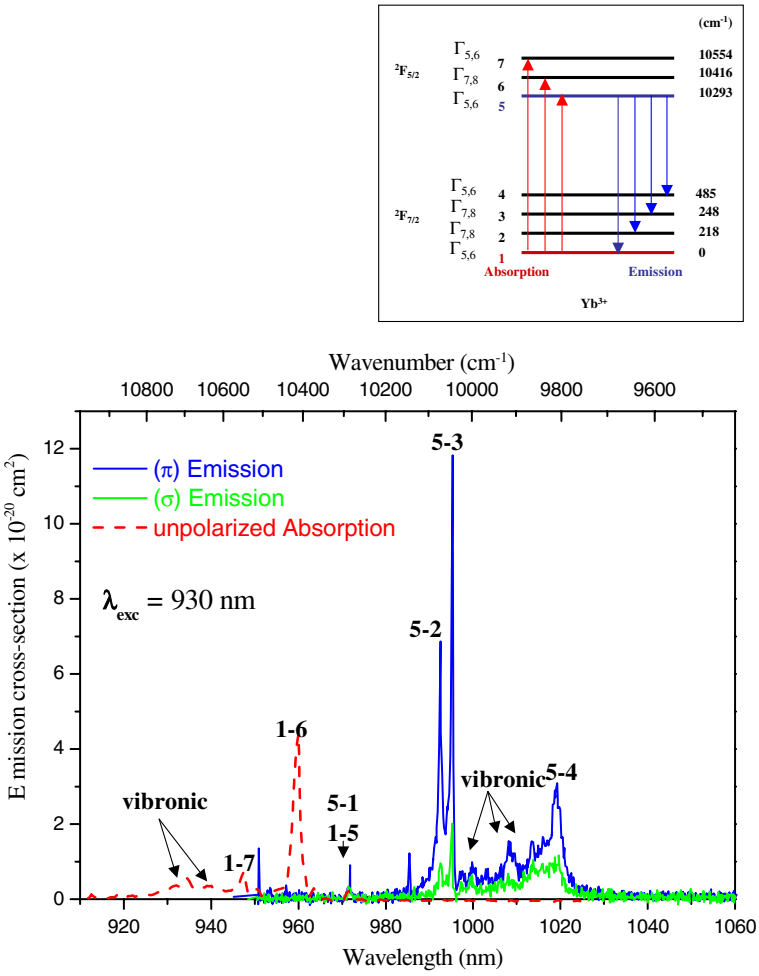

Fig. 6. Polarized absorption and emission cross-sections at 12 K of 0.5% Yb-doped $YLiF_4$.

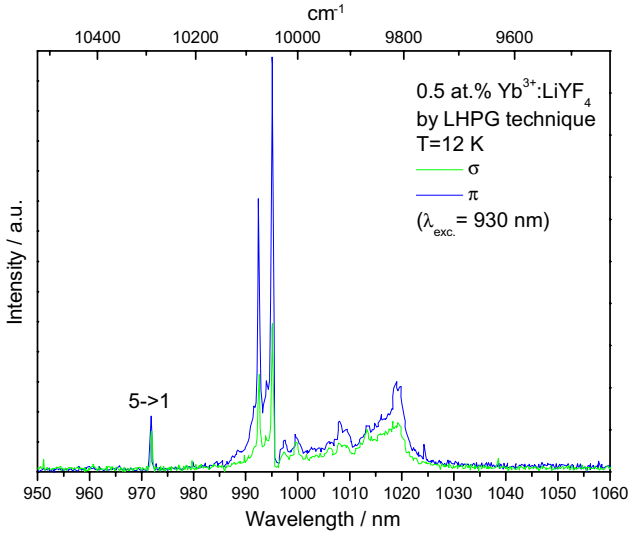

Fig. 7. Polarized absorption and emission cross-sections at 12 K of 0.5% Yb-doped $YLiF_4$ grown by the LHPG technique.

distinguish which peak corresponds to the electronic transition, polarized absorption spectra are needed at low temperature. Unfortunately our set-up allows it only at room temperature and so as it was mentioned before, the low temperature absorption spectrum shown in Fig. 5 is not polarized. Hopefully, Lupei et al. [16] show the polarized absorption spectra for the 20% Yb:YLF at 10 K and they assign the level 7 at 10 559 cm^{-1} in agreement with Morrison et al. who position this level at 10 554 cm^{-1}. As a result, it is highly probable that the $1 \rightarrow 7$ electronic transition is located at 10 554 cm^{-1} (Fig. 6) and that all the other features at higher energy have to be associated to vibronic transitions of the $1 \rightarrow 7$ electronic one since they disappear in π polarization together with the $1 \rightarrow 7$ peak [16].

3.2.2.2. Emission spectra. The $5 \rightarrow 2$ electronic emission transition do not correspond to any Raman lines thus it seems valuable to consider that the level 2 is situated at 218 cm^{-1} (emission line at 10 074 cm^{-1} at 12 K). Regarding the most intense peak of the emission spectra located at 248 cm^{-1} in Fig. 5 (emission line at 10 047 cm^{-1} at 12 K), we suppose that it corresponds to the $5 \rightarrow 3$ emission transition. This assumption would be

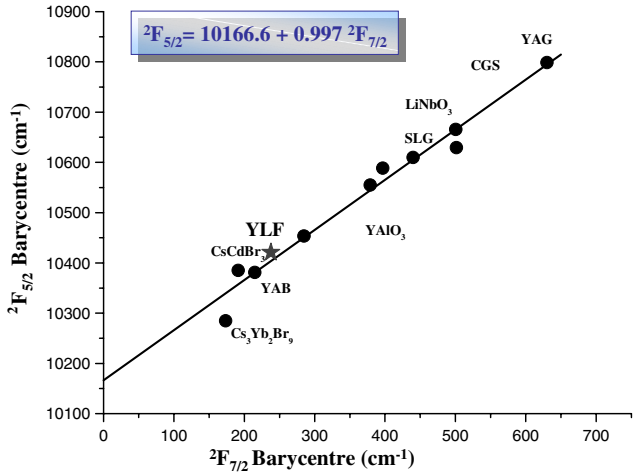

Fig. 8. Barycentre plot for various Yb^{3+}-doped materials.

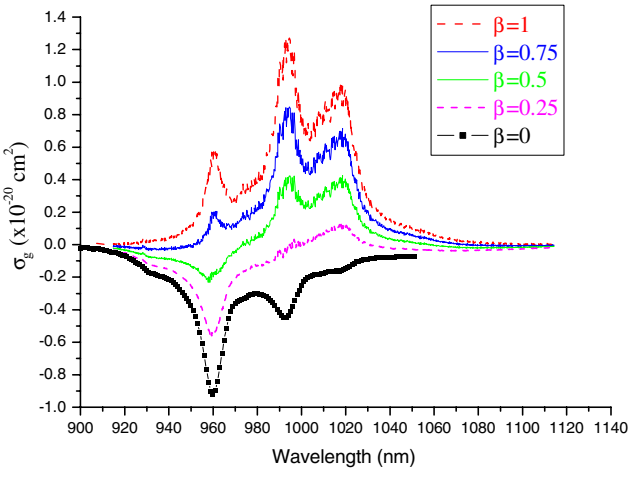

Fig. 9. Gain cross-sections curves σ_g for Yb^{3+}-doped $YLiF_4$.

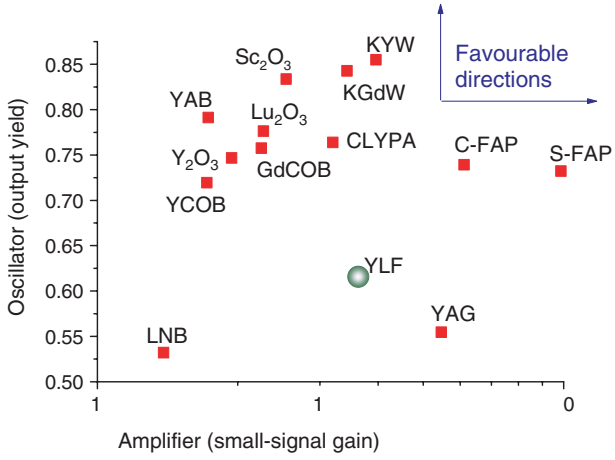

Fig. 10. Evaluation of laser output yield and amplifier small signal gain predicted by the Figure-of-Merit for $YLiF_4$.

then in agreement with almost all Yb^{3+}-doped crystals where the level 3 is the usual terminal level of the laser transition. In this particular case, this line coincides with a Raman line at 248 cm^{-1} showing that this electronic transition has also a vibronic character. We can add that the proximity of the 2 and 3 stark levels was also observed in Yb^{3+}-doped YAG [17]. The additional weak emission peaks in the range of 250–450 cm^{-1} coincide exactly with intense Raman lines so that these small peaks are probably vibronic lines of all $5\rightarrow1$, $5\rightarrow2$ and $5\rightarrow3$ transitions. Nevertheless, Morrison et al. have interpreted the $5\rightarrow3$ emission transition at 371 cm^1 (9921 cm^{-1}) which is one of the weakest lines in our measured emission spectra at 12 K and has been considered as vibronic line in our case. This difference in the interpretation might be due to the fact that Morrison et al. recorded the emission spectra at 77 K while we measured the emission at 12 K that allows a better resolution of the peak centred around 990 nm. Indeed, at 12 K it is clearly seen that this peak is composed of two peaks, which are assumed to be the $5\rightarrow2$ and $5\rightarrow3$ transitions as mentioned above. The last line of notable intensity in the emission spectrum at 1019 nm, do not overlap with a Raman line and can be characterized by the $5\rightarrow4$ transition in agreement with Morisson et al.

Furthermore after Lupei et al. [16] the representations of the Stark levels are ordered as followed $\Gamma_{5,6}$, $\Gamma_{7,8}$ and $\Gamma_{5,6}$ for the $^2F_{5/2}$ excited state and, $\Gamma_{5,6}$ for lowest Stark level of the ground state $^2F_{7/2}$. Considering both the low temperature polarized emission spectra and the selection rules for the electric-dipole transitions which are the dominant ones in the S4 non-centrosymmetric local symmetry, the representations of remaining Stark levels of $^2F_{7/2}$ are $\Gamma_{7,8}$, $\Gamma_{7,8}$ and, $\Gamma_{5,6}$. Indeed, the most intense lines in π-polarized emission spectrum correspond to the $5\rightarrow2$ and $5\rightarrow3$ transitions. Thus the nature of $5\rightarrow4$ transition should have a dominant magnetic-dipole character.

As a result of this interpretation an attempt of the Yb^{3+} energy level scheme in YLF is summarized in the inset of Fig. 6.

3.2.3. Attempt of verification by the barycentre law and the scalar field parameters

Consequently to our interpretation of Yb^{3+} energy levels in YLF, we have then applied the barycentre plot method, introduced by Antic-Fidancev [18], based on the fact that the spin orbit splitting between $^2F_{7/2}$ and $^2F_{5/2}$ is host independent, and equal to the free-ion energy separation. For rare earth ions, it was shown that the $^{2S+1}L_J$ level barycentre as a function of any other barycentre of isolated level in the $4f^n$ ground configuration, exhibits a linear dependence within the experimental errors. Especially for Yb^{3+}-doped crystals, when taking the lowest Stark level as the origin of energy and plotting the $^2F_{5/2}$ manifold energy barycentre versus the $^2F_{7/2}$ one, the representative points generally describe a

straight line characterized by a slope of unity. In the case of ytterbium, the energy separation between the two manifolds is about 10 200 cm^{-1}. We can neglect the J-mixing to a good approximation and consider constant this energy whatever the host. The $^2F_{5/2}$ level barycentre as a function of the $^2F_{7/2}$ level barycentre for several hosts is presented in Fig. 7. Plot According to the assignment of Stark levels of Yb^{3+} in YLF, we have placed this laser host on the barycentre plot and it fits well to the model.

We also tried to apply another method to check the correctness of our assignment by using the scalar field parameter N_v introduced by Auzel [19]. Using the scalar field parameter N_v, calculated from the respective B_q^k parameters given in the literature for 115 different rare earth-doped crystals, Auzel has shown that a simple linear relationship between the number of f electrons and the crystal field strength can be found. From this result, the maximum splitting of the Yb^{3+} $^2F_{7/2}$ ground state has been derived, assuming the knowledge of the maximum splitting of the Nd^{3+} $^4I_{9/2}$ ground state. Because Nd^{3+} is less prone than Yb^{3+} to mix with vibronics, this approach should help to distinguish the highest Stark level of $^2F_{7/2}$ from vibronics, using the following prediction: the maximum splitting of the $^2F_{7/2}$ Yb^{3+} ground state in a given host site cannot be less than the one of Nd^{3+} $^4I_{9/2}$ in the same crystal host site. For any crystal $\Delta E(Yb^{3+}, 7/2) > \Delta E(Nd^{3+}, 9/2)$ and the theoretical equation given is $\Delta E(Yb^{3+}, 7/2) = 1.46\ \Delta E(Nd^{3+}, 9/2)$ [20]. One prediction claims that when the opposite is experimentally found, there is a risk that vibronics have been mistaken for electronic lines. In the case of YLF host, the experimental splitting of the Nd^{3+} $^4I_{9/2}$ ground state has been studied by different authors who found similar results: 528 [21,22], 523 [23] and 524 cm^{-1} [24], respectively. Thus, according to this model, the Yb^{3+} $^2F_{7/2}$ maximum splitting should be of 775 cm^{-1} which fixes the position of the $5 \leftrightarrow 4$ transition at around 1051 nm. However, in the experimental emission spectra at 12 K recorded up to 1080 nm we could not observe any peak above 1020 nm and, consequently, we consider the $5 \rightarrow 4$ transition at this last position, giving splitting value of 486 cm^{-1}. This means that the signal detected at RT in this spectral range as reported in Fig. 3 should have a vibronic origin. Already, in his recent paper, Auzel [18] mentioned a large difference between prediction and experience for YLF, so that discrepancy between experimental and theoretical results in Yb^{3+}:YLF have to be understood.

3.3. First estimations of the laser potentialities

Using the known relationship between absorption and emission cross-sections by the following equation:

$$\sigma_g(\lambda) = \beta\sigma_{em}(\lambda) - (1-\beta)\sigma_{abs}(\lambda)$$

The gain cross-section $\sigma_g(\lambda)$ versus wavelength λ at different population inversion β can be deduced, in order to have an idea about the laser potentiality of any laser host.

In the case of Yb^{3+}-doped YLF, using the π polarization, in which both absorption and emission cross-sections are the highest (Fig. 3), the gain cross-sections were calculated.

The results presented in Fig. 8, show that for $\beta = 0.5$ the gain cross-section is positive from 980 to 1030 nm. These results are comparable to those of the reference laser materials Yb^{3+}-doped YAG garnet or Yb^{3+}-doped CFAP apatite. Moreover, the interest of YLF is to exhibit broader band-widths in contrast especially with the narrow lines of CFAP [25] which should be an advantage to avoid any derive of the diode pumping source. In the case of laser application, from the gain cross-section behaviour, the pumping wavelength should be at 960 nm (transition $1 \rightarrow 6$), whereas the predicted tunable laser wavelength could be above 1000 nm, most probably around 1020 nm where re-absorption is the weakest one.

On an other hand and according to the new evaluation of Figure-of-Merit, developed in the latest years by our group, based on a quasi-three level laser model [4,26,27], several Yb^{3+}-doped laser crystals have been evaluated. This new evaluation has been applied for both CW and amplifier regimes by using the quasi-three level laser dealing with gaussian waves, taking into account, the saturation of the absorption of the pump, the stimulated emission at the pump wavelength, the variation of the laser diode pump, the laser waists and the variation of the laser intensity along propagation. The results of calculations are visualized in Fig. 9 in a two-dimensional diagram considering the laser extracted power and the slope efficiency. According to this model a first estimation of the potentiality of Yb^{3+}-doped YLF as laser material in the IR shows that this fluoride could be almost comparable to the well known YAG laser host for application as amplifier with a higher output yield. In reality YLF has a smaller thermal conductivity which is naturally a disadvantage, however, this laser host presents the advantage of better non-linear behaviour during high power pumping action due to fluoride host nature instead of oxide one and at the end, of the large size crystal growth possibility (Fig. 10).

4. Conclusion

High optical quality crystals of Yb^{3+}-doped YLF single crystal were grown by the CZ method. Assignment of the Yb^{3+} energy levels in YLF was difficult because of the re-absorption feature in this fluoride host as well as the strong phonon–electron coupling of Yb^{3+} ion. Using absorption, emission and Raman spectroscopy measurements at RT and 12 K, an attempt of

Yb^{3+} energy levels assignment was proposed. It was not in a good agreement with the only one previous interpretation of Yb^{3+} energy levels in YLF as discussed in this work. We tried to verify our interpretation by two independent methods, the barycentre law and the scalar field parameter method. Finally, the evaluation of Yb^{3+}-doped YLF by one type of Figure-of-Merit, developed previously, shows its potentiality as laser material with the complementary advantage to be grown with large size. Laser tests should be carried out to confirm our first estimation. Similar spectroscopic investigations as well as concentration quenching in the isostructural fluoride host Yb^{3+}-doped $LuLiF_4$ are under investigation and will be submitted later.

References

[1] T.Y. Fan, IEEE J. Quantum Electr. 29 (1993) 1457.
[2] P. Lacovara, H.K. Choi, C.A. Wang, et al., Opt. Lett. 16 (1991) 1089.
[3] G. Boulon, A. Brenier, L. Laversenne, Y. Guyot, C. Goutaudier, M.T. Cohen-Adad, G. Métrat, N. Muhlstein, J. Alloy. Compd. 341 (2002) 2.
[4] A. Brenier, G. Boulon, J. Alloy. Compd. 210 (2001) 323; A. Brenier, G. Boulon, Europhys. Lett. 55 (2001) 647.
[5] J.S. Shah, in: B.R. Pamplin (Ed.), Crystal Growth and Characterisation, 6, Pergamon Press, Oxford, 1975, p. 144.
[6] R. Gaume, P. Haumesser, E.A. Fidancev, P. Porcher, B. Viana, D. Vivien, J. Alloy. Compd. 341 (2002) 160.
[7] R.D. Shanon, Acta Crystallogr. A 32 (1976) 751.
[8] L.D. de Loach, S.A. Payne, L.L. Chase, L.K. Smith, W.L. Kway, W.F. Krupke, IEEE J. Quantum Electr. 29 (1993) 1179.
[9] A. Lupei, V. Enaki, V. Lupei, C. Presura, A. Petraru, J. Alloy. compd. 275–277 (1998) 196.
[10] A. Lupei, Opt. Mater. 16 (2001) 153.
[11] G. Boulon, L. Laversenne, C. Goutaudier, Y. Guyot, M.T. Cohen-Adad, J. Lumin. 102–103 (2003) 417.
[12] P.C. Becker, G.M. Williams, N.M. Edelstein, J.A. Konigstein, L.A. Boatner, M.M. Abraham, Phys. Rev. B 45 (1992) 5027.
[13] A. Ellens, H. Andres, A. Meijerink, G. Blasse, Phys. Rev. B 55 (1997) 173.
[14] C.A. Morrison, R.P. Leavitt, in: K.A. Gschneider, L. Eyring (Eds.), Handbook on the Physics and Chemistry of Rare Earth, vol. 5, North Holland, Amsterdam, 1982, p. 461.
[15] E.A., Brown, Harry Diamond laboratories Reports TR-1932 and TR-1934 (NTIS #091 252 and 090 976), 1980.
[16] A. Lupei, V. Lupei, C. Presura, V.N. Enaki, A. Petraru, J. Phys.: Condens. Mat. 11 (1999) 3769.
[17] A. Yoshikawa, G. Boulon, L. Laversenne, H. Canibano, K. Lebbou, A. Collombet, Y. Guyot, T. Fukuda, J. Appl. Phys. 94 (2003) 5479.
[18] E. Antic-Fidancev, J. Alloy. Compd. 300–301 (2000) 2.
[19] F. Auzel, J. Lumin. 93 (2) (2001) 129.
[20] F. Auzel, Opt. Mater. 19 (1) (2002) 89.
[21] D.E. Wortman, J. Phys. Chem. Solids 33 (1971) 311.
[22] A.L. Harmer, A. Linz, D.R. Gabbe, J. Phys. Chem. Solids 30 (1969) 1483.
[23] A.A.S. de Gama, G.F. de Sa, P. Porcher, P. Caro, J. Chem. Phys. 75 (1981) 2583.
[24] H. De Leebeeck, C. Groller-Warland, J. Alloy. Compd. 225 (1995) 75.
[25] P.H. Haumesser, R. Gaumé, B. Vianna, D. Vivien, J. Opt. Soc. Am. B 19 (2002) 2365.
[26] G. Boulon, Opt. Mater. 22 (2) (2003) 85.
[27] A. Brenier, J. Lumin. 92 (3) (2001) 199.